

ARTICLE OPEN



Nanoscopic and in-situ cross-sectional observations of Li-based conversion coating formation using liquid-phase TEM

A. Kosari¹, F. Tichelaar², P. Visser³, P. Taheri¹, H. Zandbergen², H. Terryn⁴ and J. M. C. Mol¹✉

Lithium salts have been proposed as promising environmentally friendly alternatives to carcinogenic hexavalent chromium-based inhibitors for the corrosion protection of aerospace aluminium alloys (AAs). Incorporated into organic coatings, lithium salts are released at damaged locations to establish a conversion layer in which distinct sublayers have different barrier characteristics. Thus, detailed knowledge on the sequence of formation events from the early stages of nucleation towards the final multi-layered arrangement is essential for developing and optimising lithium-leaching technology for protective coatings. Here, liquid-phase-transmission electron microscopy (LP-TEM) is employed to observe nanoscopic morphological evolutions in situ during the lithium-based conversion process of AA2024-T3. Thanks to dedicated preparation of delicate sandwiched TEM specimens allowing us to explore the events cross-sectionally, we provide real-time direct mechanistic information on the conversion process from the initiation to an advanced growth stage. In parallel, we perform supplementary ex situ SEM and TEM investigations to support and validate the LP-TEM findings. The unprecedented experimental approach developed and executed in this study provides an inspiring base for studying also other complicated surface conversion processes in situ and at the nanoscopic scale.

npj Materials Degradation (2021)5:40; <https://doi.org/10.1038/s41529-021-00189-y>

INTRODUCTION

Aerospace aluminium alloys (AAs) are highly susceptible to local corrosion attack¹, thus demanding reliable, efficient and active protection during their service life². However, the highly complex microstructure of AAs, leading to enhanced mechanical properties³, brings along complicated corrosion mechanisms that make effective inhibition challenging^{4–9}. For decades, reliable active protection has been fulfilled by the application of hexavalent chromate-based conversion and organic coatings^{10–13}. However, being recognised to be toxic and carcinogenic, the urgent need has risen to replace them by non-toxic systems due to increasingly strict international health and safety legislation¹⁴. Thus, there has been a growing attention in the development of alternative systems that are not only eco-friendly but also provide reliable and long-lasting corrosion protection.

Up to now, several chromate-free conversion systems that are potentially worthy of consideration for industrial applications have been introduced, thanks to dedicated and extensive research¹⁵. Categorized according to the dominant chemistry, trivalent chromium compounds^{16–18}, rare earth salts^{19–21}, mixed zirconium/titanium systems^{22,23}, lithium salts^{24,25} and transition metal oxyanion additives^{26,27} can be mentioned. Amongst these options studied, lithium salts have the merit of being potentially used as both conversion bath chemicals^{28,29} and in particular as a leaching inhibitor compound in organic coatings^{30–33}. The latter application of lithium salts has been considered promising for the future of green active corrosion protection of AAs^{34,35}. This scheme allows lithium salts embedded in organic coatings to leach into the scratched locations of organic coatings (scribe) with a long-distance throwing power³², triggering an irreversible conversion process³³. The anionic part of lithium salts like lithium carbonate can induce an alkaline environment (pH 9–11)³⁶ within the scribe where severe corrosion is expected due to instability of the

aluminium oxide passive layer under such conditions^{37,38}. However, lithium plays a critical role in the conversion process by stabilising the corrosion products, leading to the gradual formation of a conversion layer with a multi-layered arrangement^{28,39}.

The typical morphology of a Li-based conversion layer fully grown within an artificial 1 mm wide scribe in neutral salt spray environment includes a columnar outer layer and thin dense inner layer where a porous layer resides in between^{40,41}. The sublayers contribute to the corrosion protection of the underlying AA substrate differently and as reported⁴², the dense inner layer, which has in fact the lowest porosity, offers the best protective contribution among the different sublayers. In terms of chemical composition, the outer columnar layer is composed of mostly crystalline lithium–aluminium layered double hydroxide (Li–Al LDH) while the dense inner layer contains amorphous lithium-pseudoboehmite; a mixture of both amorphous and crystalline products is found in the porous layer⁴⁰.

Up to now, a good understanding in relation to structure, morphology and composition of the conversion layer has been acquired. However, a detailed knowledge on the sequence of formation events from the early stages of nucleation towards the final multi-layered arrangement is still missing. This is of pivotal importance to understand the mechanism involved in the lithium-based conversion process and its further development towards a sustainable active protection technology with optimal reliability. Thus, an approach that can provide direct and real-time morphological observations of the entire conversion process at high temporal and spatial resolution is crucial.

To this aim, liquid-phase-transmission electron microscopy (LP-TEM)^{43–46} can be considered to observe dynamic morphological changes at AA surfaces as a consequence of interactions with a Li-based solution. However, one of the great challenges in this

¹Department of Materials Science and Engineering, Delft University of Technology, Delft, The Netherlands. ²Kavli Institute of Nanoscience, Delft University of Technology, Delft, The Netherlands. ³AkzoNobel, Sassenheim, The Netherlands. ⁴Department of Materials and Chemistry, Research Group Electrochemical and Surface Engineering (SURF), Vrije Universiteit Brussel, Brussels, Belgium. ✉email: J.M.C.Mol@tudelft.nl

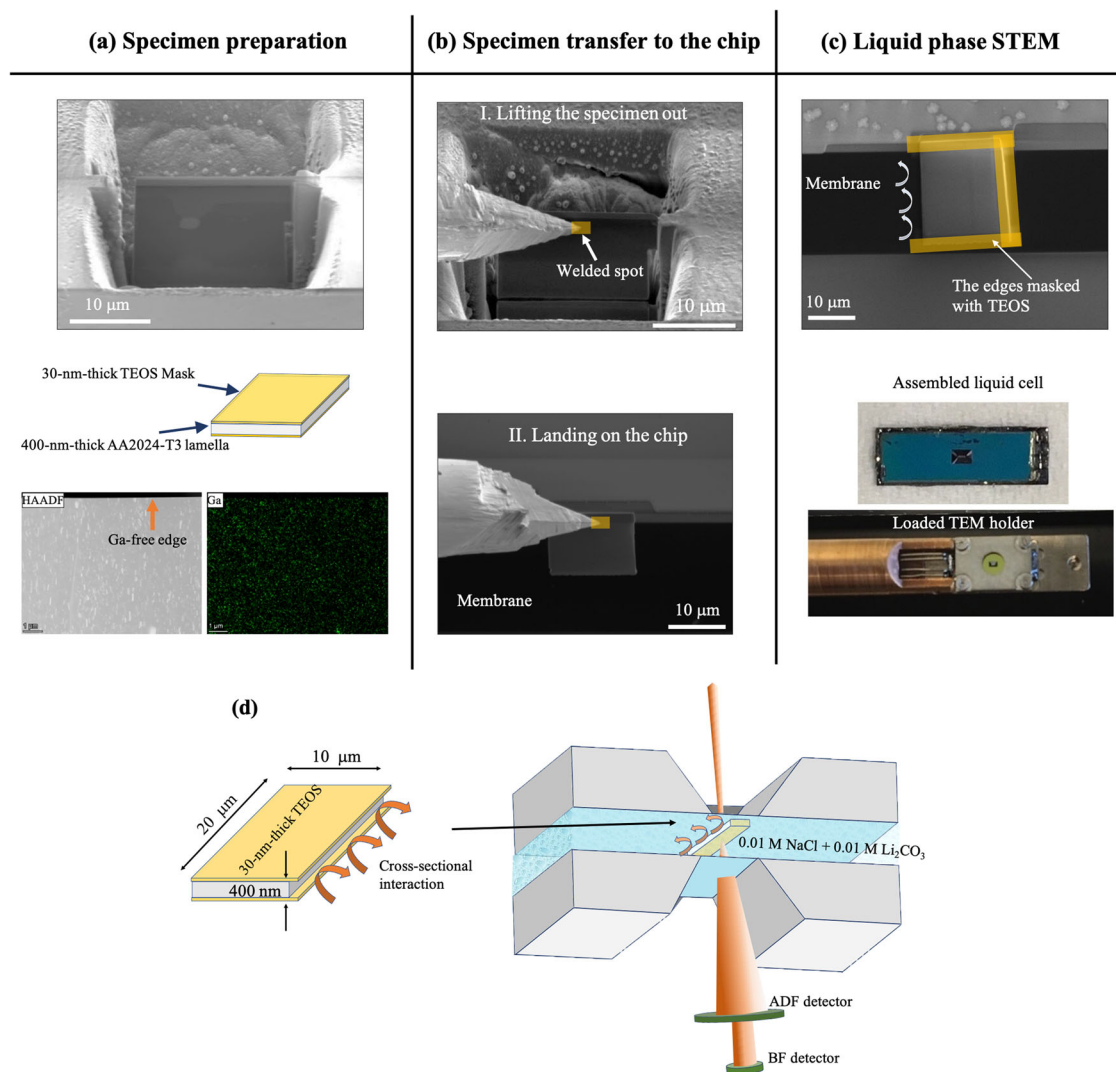


Fig. 1 Liquid-phase STEM study of Li-based conversion coating formation using sandwiched thin specimens. **a** The lamellae of 400 nm thickness are fabricated out of AA2024-T3 sheets using a Ga ion FIB/SEM. Afterwards, the prepared specimens are sandwiched by applying two 30 nm thick layers of TEOS to control the oxidation direction. The sandwiched thin specimens control the oxidation direction to be in the plane of the specimen allowing for cross-sectional observation of the conversion process. The STEM image and the corresponding Ga map shows a sandwiched lamella with a clean (Ga-free) edge to interact with the electrolyte. **b** The sandwiched lamella is transferred carefully and precisely to the chips. **c** When positioned on the chip, three other edges of the lamella are masked with TEOS, leaving the clean edge bare only. The put-together chips are sealed with an epoxy resin glue and the tip of a home-made liquid TEM holder with a loaded liquid cell is shown. **d** The experiments are performed in scanning TEM mode using either a bright-field or a high-angle annular dark-field detector. The specimen is also located at the entrance side of the liquid cell to lessen the impact of the beam-broadening caused by the thick electrolyte.

regard and related to the current work is that the TEM specimens (lamellae) require electron transparency and generally consist of foils of roughly 50–400 nm thickness. On the other hand, once the still relatively thin specimens are exposed to an aggressive environment (e.g. alkaline solutions for aluminium and its alloys), they may dissolve very quickly. Therefore, without any dedicated specimen preparation, the conversion process in which the aqueous Li-based solution dissolves a part of the metal surface to form a chemically mixed layer cannot be fulfilled. Thus, sandwiching thin specimens between inert cover layers can be a remedy in this case as the oxidation direction can be controlled to take place in the plane of the specimen rather than perpendicular to it, i.e. through-thickness. For such sandwiched specimens, the interaction initiates at the side of the thin-masked lamellae where it can penetrate cross-sectionally. This approach was employed successfully for cross-sectional LP-TEM observations of intermetallic phase-induced local corrosion in AAs⁴⁷.

This study is devoted to elucidating the formation mechanism of a protective conversion coating from a Li-salt-based solution in space and time. Here, we therefore employ a purposeful specimen masking procedure and also an intricate sample preparation and transfer-to-liquid-cell procedure for dedicated in situ LP-TEM analysis (Fig. 1). The application of liquid-phase TEM for studying sandwiched thin specimens enables to uniquely visualise the cross-sectional sequence of events with the required spatial and temporal resolution to resolve the formation mechanism from early-stage formation to the final multi-layered arrangement.

RESULTS

LP-TEM studies of the conversion layer formation

Figure 2 shows snapshots taken at different stages of the conversion layer formation at the side of a sandwiched lamella. The BF-STEM image at 0 min shows that the lamella contains three

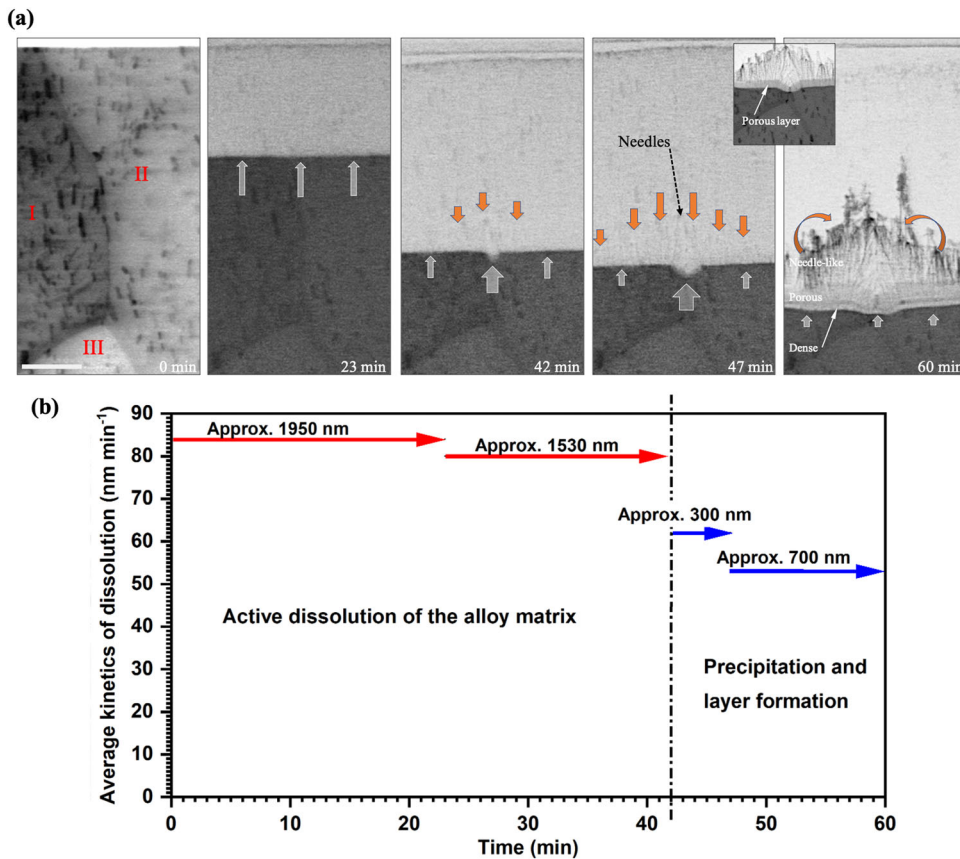


Fig. 2 Cross-sectional liquid-phase STEM observations of the conversion layer formation in 0.01 M NaCl + 0.01 M Li₂CO₃. **a** Time-resolved BF-STEM images of the conversion layer at different stages of the formation at the bare side of a sandwiched lamella. The image taken at 0 min is in the absence of the electrolyte, revealing three grains in the specimen. The process begins by uniformly dissolving the alloy until needles appear at the solution/alloy interface. A mature conversion layer including the columnar and porous layer is observed after 60 min. The inset is a closer look at the conversion layer taken at 55 min. The white and orange arrows indicate the dissolution and precipitation process, respectively. The specimen is approximately 400 nm thin excluding the TEOS layers. The scale bar is 1 μ m. **b** The graph presents the average kinetics of the alloy matrix dissolution at different stages of the conversion process.

grains. This BF-STEM image has been acquired in the absence of electrolyte; note that water causes multiple scattering of the electrons leading to a diminished contrast⁴⁸. After 23 min of exposure, we see an active dissolution of the alloy matrix without any sign of conversion layer formation. Until the total exposure of 42 min, the corrosion continues to further dissolve the alloy matrix; approximately 3.48 μ m of the specimen is dissolved totally up to this point. At 42 min, initial precipitation of the conversion layer in the form of tiny needles is observed, indicated by the orange arrows. Interestingly, the preliminary precipitation takes place when enhanced dissolution is seen in the dissolution front due to the locally dissolved matrix at the grain boundary^{49,50}. As the corrosion further propagates into the sandwiched specimen, the needles increase in number and to an average length of approximately 0.8 μ m (at 47 min). The inset allows a closer look at the layer after 55 min, revealing the formation of a porous layer upon further penetration of corrosion into the sandwiched specimen. The STEM image taken at 60 min reveals the conversion layer with a multi-layered arrangement. The needles, observed at the outer side of the specimen, are representative for the columnar morphology reported in prior literature⁴¹. The porous-like layer becomes darker in contrast as it gets closer to the alloy matrix. This can be linked to the less-porous morphology of the layer formed closest to the alloy matrix and at the latest stage of the conversion process. Thus, we here consider the layer near to the alloy matrix as the dense layer as reported in prior literature⁴¹. It should be noted that here we merely report on the

morphological evolutions; the sublayers might undergo structural and compositional modifications at different formation stages, but the current technique is unable to reveal them at that time itself. As shown in Fig. 2b, the kinetics of the dissolution gradually slows down upon conversion layer formation at different stages. The dissolution front has penetrated approximately 1950 nm from 0 to 23 min (84 nm min⁻¹), approximately 1530 nm from 23 to 42 min (80 nm min⁻¹), approximately 300 nm from 42 to 47 min (62 nm min⁻¹) and approximately 700 nm from 47 to 60 min (53 nm min⁻¹) in depth.

Figure 3 shows the further investigations of the very early stages of the conversion layer formation on a sandwiched specimen. At the beginning of exposure, the high-angle annular dark-field (HAADF)-STEM shows the appearance of some dents at the edge of the specimen, indicated by the white arrows ($t = 5$ min). However, the entire surface gets involved in the dissolution process and the alloy matrix starts to dissolve relatively uniformly ($t = 25$ min). Interestingly, the dissolution front (the substrate/layer interface) reveals an undulating pattern that shows temporary local anodes while penetrating into depth. Besides, the nanoscopic intermetallic particles (IMPs) are revealed as the bright spots in the HAADF-STEM image) that are distributed over the alloy matrix also undergo local corrosion; i.e. de-alloying possibly followed by self-corrosion of the IMP remnant leading to either complete dissolution or leaving behind bright remnants as indicated by the red arrows. Complete dissolution of the IMPs may occur once the de-alloyed IMPs (remnants) are undercut and

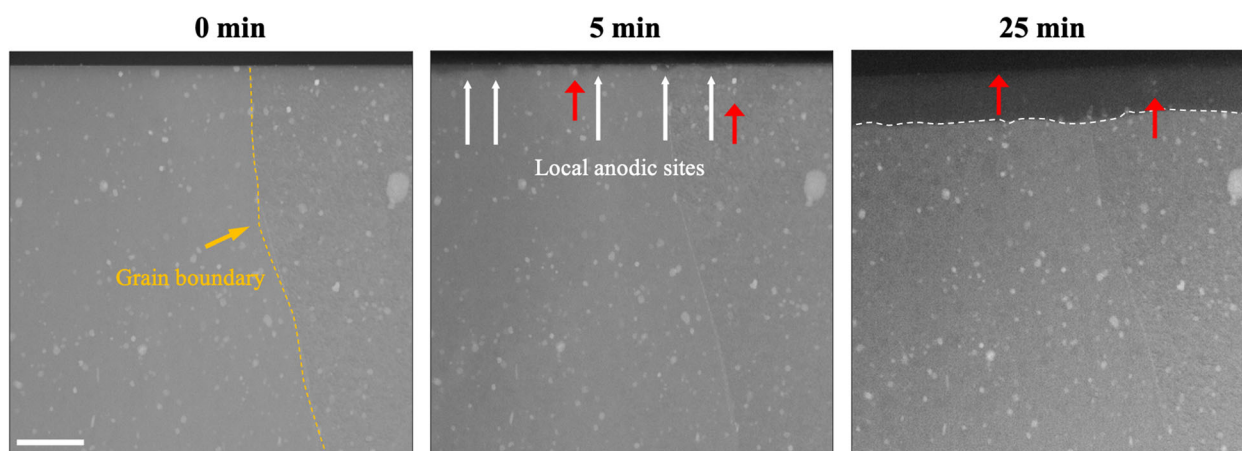


Fig. 3 LP-TEM observations of initial stages of the conversion layer formation in 0.01 M NaCl + 0.01 M Li₂CO₃. Time-resolved HAADF-STEM images of a sandwiched specimen, showing initial local anodes and then the subsequent uniform dissolution. The white arrows indicate initial local dissolution sites. The red arrows point to the nanoscopic copper-rich IMP as the potential cathodic sites. The specimen is approximately 300 nm thin excluding the TEOS layers. The scale bar is 1 μm.

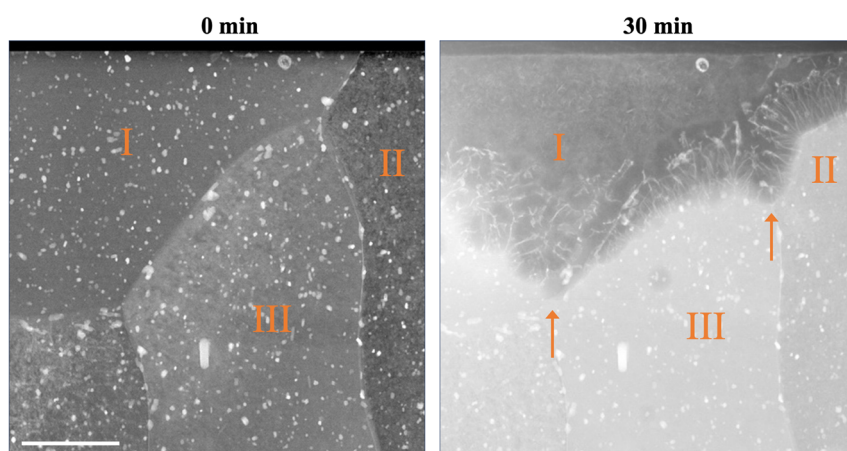


Fig. 4 LP-TEM observations of initial stages of the conversion layer formation in 0.01 M NaCl + 0.01 M Li₂CO₃. HAADF-STEM images of a sandwiched lamella before and after 30 min exposure, revealing different electrochemical activity of grain boundaries (orange arrows) and also grains. The images are taken in the absence of the electrolyte. The specimen is approximately 350 nm thin excluding the TEOS layers. The scale bar is 2 μm.

detached from the alloy matrix due to trenching and acquire a corrosion potential at which dissolution of noble elements like copper is thermodynamically favoured⁴⁷.

Figure 4 shows the HAADF-STEM images of a sandwiched specimen including three grains being involved in the conversion layer formation. Having been exposed for 30 min, we clearly see the formation of the needles while the porous layer is still absent. Note that the images are taken in the absence of the electrolyte; see more evidence in Supplementary Fig. 1. This is consistent with the real-time LP-TEM observations shown in Fig. 2, revealing the needle-like structure as the preceding morphology. As can be seen, grain I shows higher electrochemical activity and is dissolved to a greater extent, as compared to grain II. This phenomenon can be linked to specific atomic planes that dissolve at a faster rate; this phenomenon has been observed by Visser et al. for bulk samples as well³⁶. The dissolution along the grain boundaries is accelerated as shown by the red arrows; more evidence can be found in Supplementary Figs. 2 and 3. It should be noted that the formation of the needles is a dynamic process including simultaneous dissolution of the specimen and establishment of single columns (see Supplementary Movie 1).

Figure 5 shows the post-mortem HAADF-STEM/EDS analysis of the conversion layer formed on a sandwiched lamella exposed to 0.01 M NaCl + 0.01 M Li₂CO₃ for 1 h. The HAADF-STEM image reveals three distinct sublayers, verifying that the sandwiched specimens are representative for the conversion layer formation studies. As is shown, aluminium is the main elemental contributor of the layer and it has been detected everywhere within the conversion layer. The presence of oxygen is a clear indication of the conversion layer formation where copper-rich regions originating from the corrosion of nanoscopic Cu-rich IMPs are distinguishable⁴⁷. Unfortunately, the relatively high thickness of the sandwiched specimen including the Si_xN_y membrane and mask layers hindered energy electron loss spectroscopy (EELS) studies to map lithium.

Analysis of the conversion layer on bulk samples

In order to support and validate the LP-TEM results, we conducted a similar surface conversion treatment on polished AA2024-T3 bulk samples. Figure 6a shows the corrosion-attack morphology of a sample of approximately 25 cm² exposed to 100 mL (electrolyte thickness = 40 mm) of the studied solution for 7 h. It shows that the formation of the conversion layer is delayed if the sample is

exposed to a large amount of 0.01 M NaCl + 0.01 M Li₂CO₃ solution. As evident, the corrosion-attack morphology is rather rough due to severe corrosion. Furthermore, the corresponding SEM image reveals no conversion layer formed on this sample. In

contrast, we see the formation of the conversion layer within the same period if an identical sample is exposed to 5 mL of the solution (electrolyte thickness = 2 mm). In Fig. 6b, the alloy surface is still shiny and the SEM image obviously shows the typical petal top-view morphology of the conversion layer⁴¹.

Figure 7 shows the cross-sectional STEM/EDS analysis of the conversion layer corresponding to Fig. 6b. Morphologically, the layer is composed of a columnar outer layer of 50–100 nm thickness and an underlying porous layer of the same thickness. Comparatively, the conversion layers generated from leaching of lithium carbonate within the scribe in salt spray environment are rather thicker as they are exposed to different electrolyte conditions and for a longer period (i.e. 168 h). As expected, the layer mainly contains aluminium and oxygen, implying the formation of a conversion layer. Interestingly, some bright spots are observed in the HAADF-STEM image corresponding to the elemental copper map; note the white arrows. The incorporation of lithium in the conversion layer has already been demonstrated elsewhere^{39,40}. In a prior work, we demonstrated that lithium can be found in both crystalline Li-Al LDH and amorphous compounds within the conversion layer⁴⁰.

DISCUSSION

Here, the direct LP-TEM observations along with the complementary analysis provide us with a comprehensive insight into the mechanisms of the Li-based conversion process on AAs at high temporal and spatial resolution. Figure 8 schematically shows different stages of the conversion layer formation in the sandwiched thin specimen corresponding to the bulk system. The graph schematically shows the change of the Al(OH)₄⁻ concentration (concluded from Fig. 6) and the dissolution kinetics (concluded from Fig. 2) while the conversion layer evolves morphologically.

Given the instability of an aluminium oxide passive layer in the alkaline environment (here pH 10.6)⁵¹, the active dissolution of the alloy matrix initiates at some regions of the matrix upon passivity loss. It preferably takes place at the grain boundaries or nanoscopic IMPs that have higher electrochemical activity^{47,50}. Thus, the alloy matrix undergoes active dissolution, resulting in an

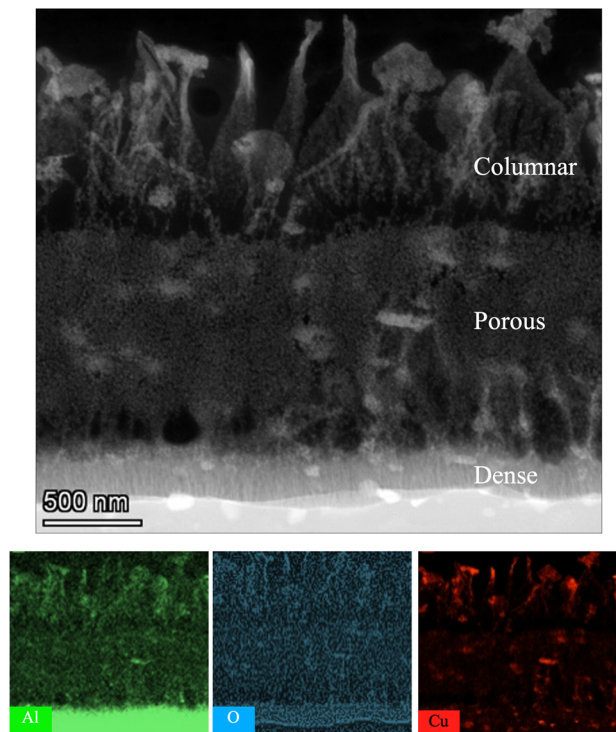


Fig. 5 Post-mortem analysis of the conversion layer formed on a sandwiched specimen in 0.01 M NaCl + 0.01 M Li₂CO₃. HAADF-STEM/EDS analysis of the preformed conversion layer, showing a multi-layered arrangement. Furthermore, Al, O and Cu are identified as main elements incorporated into the layer. Cu-rich regions are the corroded nanometric intermetallic particles. Note that lithium cannot be detected via EDS technique.

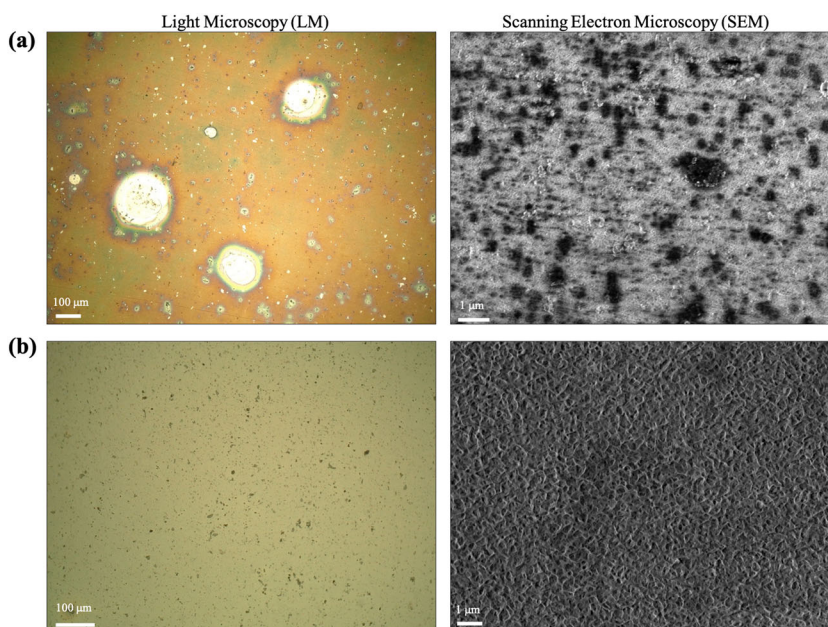


Fig. 6 Surface morphology of the AA sample exposed to different amount of 0.01 M NaCl + 0.01 M Li₂CO₃ solution for 7 h. LM and SEM images of the conversion layer formed at the batch condition of the solution volume/exposed surface area ratio of: **a** 4 mL cm⁻² and **b** 0.2 mL cm⁻².

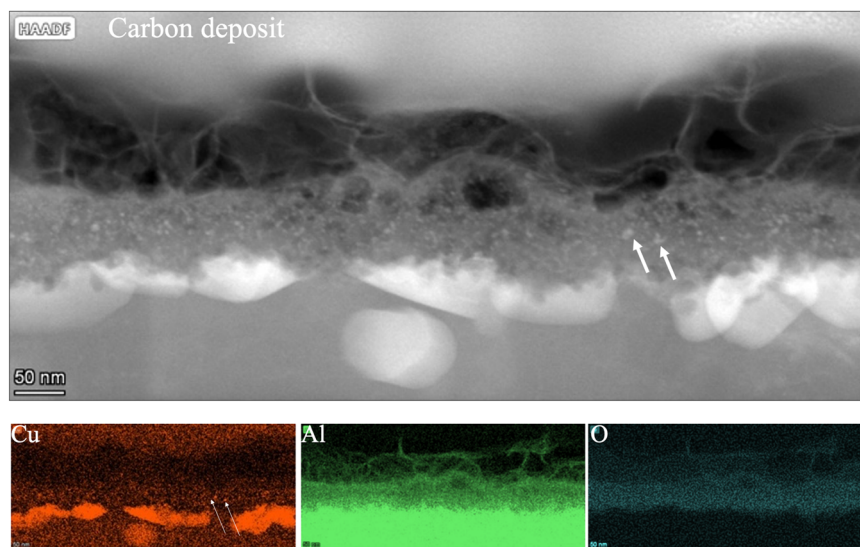


Fig. 7 Post-mortem analysis of the conversion layer formed on the bulk alloy. Cross-sectional STEM/EDS analysis of the conversion layer. The white arrows point to the copper-rich regions in the conversion layer; see the Cu map. The lamella was fabricated with the lift-out FIB procedure out of the sample exposed to 5 mL of 0.01 M NaCl + 0.01 M Li_2CO_3 solution for 7 h.

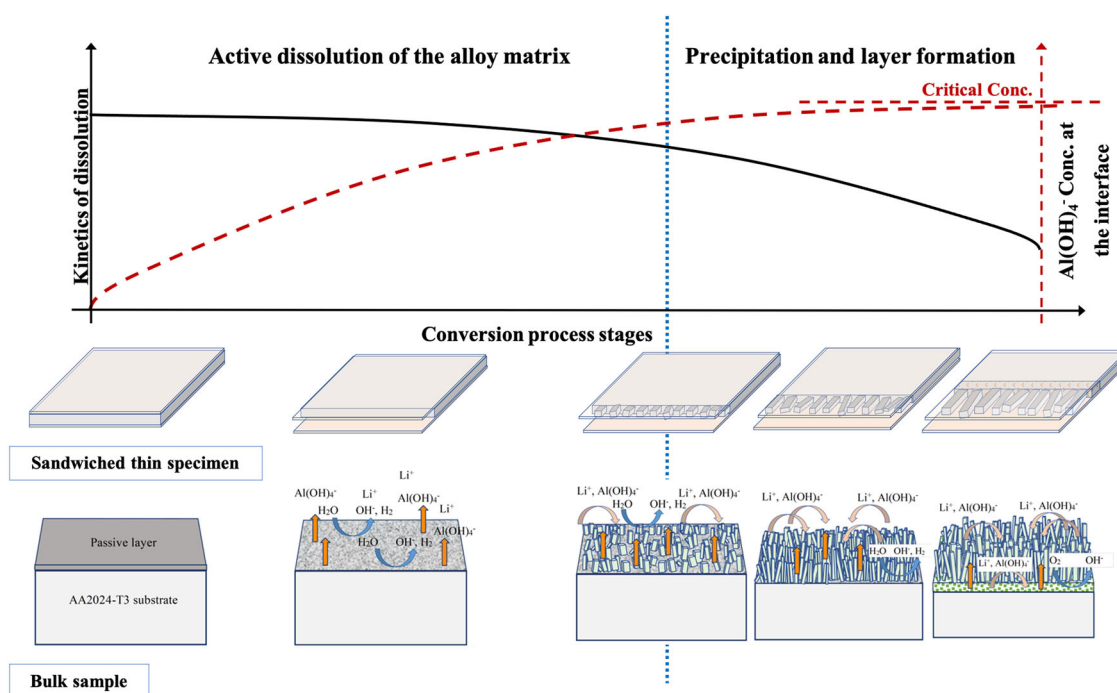


Fig. 8 Morphological stages of the lithium-based conversion layer formation. The graph schematically shows the change of the Al(OH)_4^- concentration and the dissolution kinetics while the conversion layer morphologically evolves. The pictures schematically show different stages of the conversion layer formation in the sandwiched thin specimen corresponding to the bulk system.

enhanced concentration of Al(OH)_4^- at the alloy matrix/solution interface. For the sandwiched thin specimen, the mass transfer of Al(OH)_4^- ions from the interface outwards takes place through the confined region between the layers of tetraethyl orthosilicate (TEOS). Because Al(OH)_4^- is the only soluble form in the alkaline media studied, this circumstance gives rise to a slowing effect on the dissolution kinetics of aluminium over time, especially when the dissolution front penetrates deeper, extending the diffusion line. Nevertheless, the dissolution of the alloy matrix continues until the needles appear as the first precipitates upon supersaturation.

In fact, the conversion layer appears in the form of needles as a part of the surface undergoing active dissolution while the precipitation happens in its close vicinity (see Supplementary Movie 1). As the conversion process proceeds, the Al(OH)_4^- concentration at different locations of the alloy matrix/solution interface reaches required supersaturation, leading to a higher rate of precipitation; the needles grow taller and increase in number. In fact, the substrate is the only source for supplying the main constituent element of the conversion layer that is aluminium. According to Drewien et al., supersaturation of solution by Al(OH)_4^- is critical for triggering the precipitation of

stable and protective Li-incorporated corrosion products²⁸. In the presence of lithium, the supersaturation state may require lower concentrations of $\text{Al}(\text{OH})_4^-$ as compared to the supersaturated condition in pure water. Under the experimental conditions of LP-TEM, the supersaturation can actually be fulfilled at the expense of the substrate dissolution until reaching a critical concentration of $\text{Al}(\text{OH})_4^-$. This can explain why the conversion layer formation is delayed if a larger amount of the lithium-containing solution is used as observed for the post-exposure *ex situ* microscopic analysis. Therefore, the higher solution volume needs excess dissolution of the substrate to become saturated (Fig. 6).

From this stage onwards, the conversion layer shows a porous morphology due to a supersaturated state and slower dissolution rate of the alloy matrix (higher precipitation/dissolution rate). However, the dissolution front still moves along until the formation of a sublayer which is less porous (dense-like layer), effectively slowing down the process. This phenomenon can also hinder the diffusion of dissolved ions outwards and accommodates local $\text{Al}(\text{OH})_4^-$ supersaturation in which the next sublayer consequently shows up in a less-porous morphology. Since the dense layer can act well as a protective barrier, it effectively hinders further dissolution until the conversion layer process comes to a halt. Besides, it is reasonable to assume that the pH gradually drops with distance from the surface, which can also thermodynamically favour the passivation of the alloy surface. However, the dissolution front can penetrate into depth⁵¹ as long as the local pH is above 8.

Given the prior investigations by Visser et al.³⁹ and the current observations with LP-TEM, we can correlate all the stages of the conversion process in the sandwiched thin specimens to those taking place in the bulk samples from a mechanistic point of view. As schematically shown in Fig. 8, initial stages of active dissolution are identical in both the thin and bulk system. For the sandwiched thin specimens, the required local supersaturation can however happen over shorter periods, although the sandwiched thin specimens experience a considerably larger solution amount to the exposed surface area within the liquid cell. That is caused by the confinement between two layers of TEOS that allows the thin specimens to preserve their local solution chemistry at the matrix/solution interface. Furthermore, the columns can grow in three-dimensional space in the bulk systems and become entangled over time, as opposed to two-dimensionally grown needles in the sandwiched thin specimens. This phenomenon is associated with a decelerated dissolution rate and consequently the prolonged conversion process in the bulk systems. As directly observed with LP-TEM, the dense layer is formed at the latest stages of the conversion process when the kinetics of dissolution/precipitation ratio is low; this is the case for the bulk state as well. Given the enhanced barrier properties of the dense layer, the samples exposed longer to a lithium-containing solution can thus reveal superior corrosion performance in line with prior work reported by Visser et al.³⁹. In fact, they can acquire a thicker dense layer during a longer period of exposure.

In summary, LP-TEM using the sandwiched specimens allows to study degradation and deposition processes at AA surfaces *in situ* in aggressive environments at high temporal and spatial resolution. Here, we employed that to observe, for the first time, morphological evolutions during the Li-based conversion process including different stages of the layer formation on aerospace AAs. In LP-TEM, the experimental conditions are rather different, in terms of the specimen size and solution volume from bulk systems traditionally studied, resulting in a shorter period of the conversion process. However, the sandwiched specimen can still be considered representative for morphological evolutions during different stages of the conversion process. Thanks to the sandwiched thin specimens, the solution is confined between two layers of TEOS, enhancing local supersaturation.

In this study, the required supersaturation by $\text{Al}(\text{OH})_4^-$ of the solution is found to be the key to establish the conversion layer and is formed at the expense of the dissolution of the alloy substrate. The direct nanoscopic evidence revealed that the sublayer with a columnar morphology is formed initially, precipitating upon supersaturation at local active anode sites like, firstly, at grain boundaries. It continues to grow after which the further growth appears in a porous morphology and is completed by the formation of a thin dense layer closest to the substrate. The establishment and growth of the conversion layer can lead to a higher precipitation/dissolution ratio with time, subsequently causing the formation of sublayers with less porous characteristics. The approach and the findings of the current study can be applied to study and explain layer formation mechanisms of other complicated conversion systems.

METHOD

Liquid-phase scanning TEM

We employed a Thermo-Fisher Helios G4 FIB/SEM equipped with the EasyLift NanoManipulator system to prepare the TEM specimens (lamellae) and also to transfer them to the liquid cells. Relatively thick (approximately 300–400 nm) lamellae were fabricated and masked with 30 nm thick layers of TEOS on both sides (Fig. 1a) to cross-sectionally observe the conversion layer formation. Thick specimens provide more material for the formation of the Li-based conversion layer while the resolution still remains good enough to explore nanoscopic morphological evolutions during the process. The sample transfer procedure and TEOS deposition parameters were presented in detail elsewhere⁴⁷. To transfer the specimens to the chips, the needle was welded to the prepared specimen with a 100 nm thick TEOS layer using the electron beam (Fig. 1b). Interestingly, there is no need to cut off the TEOS weld and it smoothly detaches itself upon landing the lamella on the chip and the electron transparent membrane. Note that the cut-off process using the gallium beam might result in contaminating the specimen with gallium. When positioned on the chip, the lamellae were also masked with rather thick TEOS layers on three sides, leaving the clean edge bare to interact with the electrolyte (Fig. 1c). Note that TEOS is electrochemically inactive and does not establish galvanic interaction with the AA specimen. The chips were plasma cleaned for 1 min before putting the liquid cells together to remove contaminations and to make the surfaces hydrophilic, facilitating the initial flow to fill up the liquid cell with the electrolyte⁵². It should be noted that the electrolyte was stagnant during the experiments in order to avoid disturbing the local solution chemistry during the conversion process by a flowing electrolyte. When loaded on a home-made liquid-cell TEM holder, the specimens were located at the entrance side of the electron probe to effectively mitigate the beam-broadening effect on the resolution in STEM mode (Fig. 1c)⁵³. A schematic representation of the current liquid-phase STEM research approach is shown in Fig. 1d.

A Cs corrected Thermo-Fisher Titan 300 kV TEM was employed to perform *in situ* studies. For low-dose *in situ* imaging, a bright-field (BF) detector was used as it further alleviates the beam-broadening effect and additionally has the benefit of an enhanced signal-to-noise ratio compared to a HAADF detector⁴⁸. To effectively lessen the electron beam impact on solution chemistry, a low-beam current of 0.1 nA, measured with liquid between the membranes only (no sample), was used. Besides, a few snapshots were merely taken during an experiment of 1 h. Note that the studied solution is moderately alkaline but may gradually turn acidic if it were continuously exposed to the electron beam, hence the interrupted but frequent imaging procedure is applied^{54,55}. Snapshots at critical stages were taken at 5000X magnification of 2048 × 2048 pixels. To further mitigate the electron effect regarding the point-excitation in STEM mode⁵⁶, the drift-corrected frame integration (DCFI) function on the Thermo Fisher Velox software was used to integrate three acquired frames at a low dwell time of 0.2 μs. The electrolyte, 0.01 M NaCl + 0.01 M Li_2CO_3 (pH 10.6), was stagnant during the experiment. According to the literature, this solution chemistry is representative for lithium concentration and pH in a defect area of 1 mm wide when leaching takes place from the coating matrix³⁹.

Typical SEM/TEM analysis

For ex situ analysis, 2 mm thick sheets of AA2024-T3 were polished in a 0.5 and 0.05 μm alumina slurry in a non-aqueous solution on a soft cloth, followed by cleaning with isopropanol in an ultrasonic bath. Afterwards, an area of approximately 25 cm^2 of the specimens was exposed to either 5 mL (electrolyte thickness = 2 mm) or 100 mL (electrolyte thickness = 40 mm) 0.01 M NaCl + 0.01 M Li_2CO_3 (pH 10.6) solution for 7 h. After completion of the exposure, the samples were rinsed off carefully with copious distilled water for a few seconds to avoid direct salt precipitation upon drying. Then, the surface morphology of the conversion layer formed on the alloy matrix was inspected with SEM performed at 15 keV collecting emitted secondary electrons (SE) in ultra-high-resolution mode. Besides, the thin cross-sections for TEM were fabricated out of regions-of-interest with FIB and lift-out procedure for detailed morphological and compositional investigations. Elemental analysis of the specimens was carried out with the Thermo-Fisher Super-X Detection System installed on the Titan microscope.

DATA AVAILABILITY

The authors declare that all data supporting the findings of this study are available within the paper and its Supplementary information files.

Received: 6 May 2021; Accepted: 16 July 2021;

Published online: 05 August 2021

REFERENCES

- Hughes, A. E. et al. High strength Al-alloys: microstructure, corrosion and principles of protection. In *Recent Trends in Processing and Degradation of Aluminium Alloys*, Vol. 1 (ed. Ahmad, Z.) 223–262 (IntechOpen, 2011).
- Visser, P., Terryn, H. & Mol, J. M. C. Part IV Applications: Aerospace coatings. In *Active Protective Coatings*, Vol. 1 (eds Hughes, A. E., Mol, J. M. C., Zheludkevich, M. L. & Buchheit, R. G.) 315–372 (Springer, 2016).
- Liddicoat, P. V. et al. Nanostructural hierarchy increases the strength of aluminium alloys. *Nat. Commun.* **1**, 1–7 (2010).
- Boag, A., Hughes, A., Glenn, A., Muster, T. & McCulloch, D. Corrosion of AA2024-T3 part I: localised corrosion of isolated IM particles. *Corros. Sci.* **53**, 17–26 (2011).
- Kosari, A. et al. Dealloying-driven local corrosion by intermetallic constituent particles and dispersoids in aerospace aluminium alloys. *Corros. Sci.* **177**, 108947 (2020).
- Örnek, C., Leygraf, C. & Pan, J. Real-time corrosion monitoring of aluminum alloy using scanning Kelvin probe force microscopy. *J. Electrochem. Soc.* **167**, 081502 (2020).
- Parvizi, R. et al. Probing corrosion initiation at interfacial nanostructures of AA2024-T3. *Corros. Sci.* **116**, 98–109 (2017).
- Buchheit, R., Martinez, M. & Montes, L. Evidence for Cu ion formation by dissolution and dealloying the Al_2CuMg intermetallic compound in rotating ring-disk collection experiments. *J. Electrochem. Soc.* **147**, 119 (2000).
- Frankel, G. W. R. Whitney Award Lecture: The effects of microstructure and composition on Al alloy corrosion. *Corrosion* **71**, 1308–1320 (2015).
- Campestrini, P., Terryn, H., Vereecken, J. & De Wit, J. Chromate conversion coating on aluminum alloys: III. Corrosion protection. *J. Electrochem. Soc.* **151**, B370 (2004).
- Kendig, M. & Buchheit, R. Corrosion inhibition of aluminum and aluminum alloys by soluble chromates, chromate coatings, and chromate-free coatings. *Corrosion* **59**, 379–400 (2003).
- Ilevbare, G., Scully, J., Yuan, J. & Kelly, R. Inhibition of pitting corrosion on aluminum alloy 2024-T3: effect of soluble chromate additions vs chromate conversion coating. *Corrosion* **56**, 227–242 (2000).
- Hughes, A., Taylor, R. & Hinton, B. Chromate conversion coatings on 2024 Al alloy. *Surf. Interface Anal.* **25**, 223–234 (1997).
- Saha, R., Nandi, R. & Saha, B. Sources and toxicity of hexavalent chromium. *J. Coord. Chem.* **64**, 1782–1806 (2011).
- Becker, M. Chromate-free chemical conversion coatings for aluminum alloys. *Corros. Rev.* **37**, 321–342 (2019).
- Li, L. & Swain, G. M. Effects of aging temperature and time on the corrosion protection provided by trivalent chromium process coatings on AA2024-T3. *ACS Appl. Mater. Interfaces* **5**, 7923–7930 (2013).
- Guo, Y. & Frankel, G. S. Characterization of trivalent chromium process coating on AA2024-T3. *Surf. Coat. Technol.* **206**, 3895–3902 (2012).
- Verdalet-Guardiola, X., Saillard, R., Fori, B., Duluard, S. & Blanc, C. Comparative analysis of the anticorrosive properties of trivalent chromium conversion coatings formed on 2024-T3 and 2024-T351 aluminium alloys. *Corros. Sci.* **167**, 108508 (2020).
- Forsyth, M. et al. Inhibition of corrosion on AA2024-T3 by new environmentally friendly rare earth organophosphate compounds. *Corrosion* **64**, 191–197 (2008).
- Li, J., Hurley, B. & Buchheit, R. Microelectrochemical characterization of the effect of rare earth inhibitors on the localized corrosion of AA2024-T3. *J. Electrochem. Soc.* **162**, C563 (2015).
- Denissen, P. J., Shkirskiy, V., Volovitch, P. & Garcia, S. J. Corrosion inhibition at scribed locations in coated AA2024-T3 by cerium- and DMTD-loaded natural silica microparticles under continuous immersion and wet/dry cyclic exposure. *ACS Appl. Mater. Interfaces* **12**, 23417–23431 (2020).
- Santa Coloma, P. et al. Chromium-free conversion coatings based on inorganic salts (Zr/Ti/Mn/Mo) for aluminum alloys used in aircraft applications. *Appl. Surf. Sci.* **345**, 24–35 (2015).
- Sarfraz, A., Posner, R., Lange, M. M., Lill, K. & Erbe, A. Role of intermetallics and copper in the deposition of ZrO₂ conversion coatings on AA6014. *J. Electrochem. Soc.* **161**, C509 (2014).
- Visser, P. et al. The corrosion protection of AA2024-T3 aluminium alloy by leaching of lithium-containing salts from organic coatings. *Faraday Discuss.* **180**, 511–526 (2015).
- Visser, P., Terryn, H. & Mol, J. M. Active corrosion protection of various aluminium alloys by lithium-leaching coatings. *Surf. Interface Anal.* **51**, 1276–1287 (2019).
- Madden, S. B. & Scully, J. R. Inhibition of AA2024-T351 corrosion using permanganate. *J. Electrochem. Soc.* **161**, C162 (2014).
- Hughes, A., Gorman, J., Harvey, T., Galassi, A. & McAdam, G. Development of permanganate-based coatings on aluminum alloy 2024-T3. *Corrosion* **62**, 773–780 (2006).
- Drewien, C., Eatough, M., Tallant, D., Hills, C. & Buchheit, R. Lithium-aluminum-carbonate-hydroxide hydrate coatings on aluminum alloys: composition, structure, and processing bath chemistry. *J. Mater. Res.* **11**, 1507–1513 (1996).
- Buchheit, R. G., Bode, M. & Stoner, G. Corrosion-resistant, chromate-free talc coatings for aluminum. *Corrosion* **50**, 205–214 (1994).
- Laird, J. S. et al. Li leaching from lithium carbonate-primer: an emerging perspective of transport pathway development. *Prog. Org. Coat.* **134**, 103–118 (2019).
- Marcoen, K. et al. Compositional study of a corrosion protective layer formed by leachable lithium salts in a coating defect on AA2024-T3 aluminium alloys. *Prog. Org. Coat.* **119**, 65–75 (2018).
- Visser, P. et al. The chemical throwing power of lithium-based inhibitors from organic coatings on AA2024-T3. *Corros. Sci.* **150**, 194–206 (2019).
- Visser, P., Terryn, H. & Mol, J. M. On the importance of irreversibility of corrosion inhibitors for active coating protection of AA2024-T3. *Corros. Sci.* **140**, 272–285 (2018).
- Visser, P. & Hayes, S. Low-temperature-curable coating composition useful as anticorrosive primer coating for non-ferrous metal substrates, particularly aluminum or aluminum alloy, comprises film-forming resin, curing agent, and lithium salt. Patent WO2010112605-A1 (2010).
- Gharbi, O., Thomas, S., Smith, C. & Birbilis, N. Chromate replacement: what does the future hold? *npj Mater. Degrad.* **2**, 1–8 (2018).
- Visser, P., Lutz, A., Mol, J. & Terryn, H. Study of the formation of a protective layer in a defect from lithium-leaching organic coatings. *Prog. Org. Coat.* **99**, 80–90 (2016).
- Tabrizi, M., Lyon, S., Thompson, G. & Ferguson, J. The long-term corrosion of aluminium in alkaline media. *Corros. Sci.* **32**, 733–742 (1991).
- Burstein, G. & Cinderey, R. Evolution of the corrosion potential of repassivating aluminium surfaces. *Corros. Sci.* **33**, 475–492 (1992).
- Visser, P., Gonzalez-Garcia, Y., Mol, J. M. & Terryn, H. Mechanism of passive layer formation on AA2024-T3 from alkaline lithium carbonate solutions in the presence of sodium chloride. *J. Electrochem. Soc.* **165**, C60 (2018).
- Kosari, A. et al. Cross-sectional characterization of the conversion layer formed on AA2024-T3 by a lithium-leaching coating. *Appl. Surf. Sci.* **512**, 145665 (2020).
- Liu, Y. et al. Protective film formation on AA2024-T3 aluminum alloy by leaching of lithium carbonate from an organic coating. *J. Electrochem. Soc.* **163**, C45 (2015).
- Visser, P., Meeusen, M., Gonzalez-Garcia, Y., Terryn, H. & Mol, J. M. Electrochemical evaluation of corrosion inhibiting layers formed in a defect from lithium-leaching organic coatings. *J. Electrochem. Soc.* **164**, C396 (2017).
- Chee, S. W. & Burke, M. G. Applications of liquid cell TEM in corrosion science. In *Liquid Cell Electron Microscopy* (ed. Ross, F. M.) 258–275 (Cambridge University Press, 2016).
- Kosari, A. et al. Application of in situ liquid cell transmission electron microscopy in corrosion studies: a critical review of challenges and achievements. *Corrosion* **76**, 4–17 (2020).

45. Ross, F. M. Opportunities and challenges in liquid cell electron microscopy. *Science* **350**, aaa9886 (2015).
46. Hayden, S. C. et al. Localized corrosion of low-carbon steel at the nanoscale. *npj Mater. Degrad.* **3**, 1–9 (2019).
47. Kosari, A. et al. In-situ nanoscopic observations of dealloying-driven local corrosion from surface initiation to in-depth propagation. *Corros. Sci.* **177**, 108912 (2020).
48. de Jonge, N. Theory of the spatial resolution of (scanning) transmission electron microscopy in liquid water or ice layers. *Ultramicroscopy* **187**, 113–125 (2018).
49. Wang, Z. et al. The intergranular corrosion susceptibility of 2024 Al alloy during re-ageing after solution treating and cold-rolling. *Corros. Sci.* **114**, 156–168 (2017).
50. de Bonfils-Lahovary, M.-L., Laffont, L. & Blanc, C. Characterization of intergranular defects in a 2024 T351 aluminium alloy. *Corros. Sci.* **119**, 60–67 (2017).
51. Pourbaix, M. *Atlas of Electrochemical Equilibria in Aqueous Solution*. 307 (NACE, 1974).
52. Woehl, T. J. et al. Experimental procedures to mitigate electron beam induced artifacts during in situ fluid imaging of nanomaterials. *Ultramicroscopy* **127**, 53–63 (2013).
53. De Jonge, N. & Ross, F. M. Electron microscopy of specimens in liquid. *Nat. Nanotechnol.* **6**, 695–704 (2011).
54. Schneider, N. M. Electron beam effects in liquid cell TEM and STEM. In *Liquid Cell Electron Microscopy* (ed. Ross, F. M.) 140–163 (Cambridge University Press, 2016).
55. Schneider, N. M. et al. Electron–water interactions and implications for liquid cell electron microscopy. *J. Phys. Chem. C* **118**, 22373–22382 (2014).
56. Woehl, T. & Abellan, P. Defining the radiation chemistry during liquid cell electron microscopy to enable visualization of nanomaterial growth and degradation dynamics. *J. Microsc.* **265**, 135–147 (2017).

ACKNOWLEDGEMENTS

This work is part of the research program Understanding Processes using Operando Nanoscopy (UPON) with project number 14205 (B2), which is financed by the Dutch Research Council (NWO) and partially by AkzoNobel.

AUTHOR CONTRIBUTIONS

A.K. prepared the TEM specimens and liquid cells, conducted TEM experiments, performed data analysis and wrote the main text of the manuscript. F.D. helped with

the TEM works. P.V. and P.T. helped with the data analysis. H.Z. contributed to the design of the TEM holder and liquid cell, supervised the TEM works. H.T. and J.M.C.M. contributed to developing the overall research strategy and supervised the work. All the authors read and edited the manuscript.

COMPETING INTERESTS

The authors declare no competing interests.

ADDITIONAL INFORMATION

Supplementary information The online version contains supplementary material available at <https://doi.org/10.1038/s41529-021-00189-y>.

Correspondence and requests for materials should be addressed to J.M.C.M.

Reprints and permission information is available at <http://www.nature.com/reprints>

Publisher's note Springer Nature remains neutral with regard to jurisdictional claims in published maps and institutional affiliations.



Open Access This article is licensed under a Creative Commons Attribution 4.0 International License, which permits use, sharing, adaptation, distribution and reproduction in any medium or format, as long as you give appropriate credit to the original author(s) and the source, provide a link to the Creative Commons license, and indicate if changes were made. The images or other third party material in this article are included in the article's Creative Commons license, unless indicated otherwise in a credit line to the material. If material is not included in the article's Creative Commons license and your intended use is not permitted by statutory regulation or exceeds the permitted use, you will need to obtain permission directly from the copyright holder. To view a copy of this license, visit <http://creativecommons.org/licenses/by/4.0/>.

© The Author(s) 2021